

Fracture field for large-scale ice dynamics

Torsten ALBRECHT,^{1,2} Anders LEVERMANN^{1,2}

¹Potsdam Institute for Climate Impact Research (PIK), Potsdam, Germany

E-mail: torsten.albrecht@pik-potsdam.de

²Institute of Physics, University of Potsdam, Potsdam, Germany

ABSTRACT. Recent observations and modeling studies emphasize the crucial role of fracture mechanics for the stability of ice shelves and thereby the evolution of ice sheets. Here we introduce a macroscopic fracture-density field into a prognostic continuum ice-flow model and compute its evolution incorporating the initiation and growth of fractures as well as their advection with two-dimensional ice flow. To a first approximation, fracture growth is assumed to depend on the spreading rate only, while fracture initiation is defined in terms of principal stresses. The inferred fracture-density fields compare well with observed elongate surface structures. Since crevasses and other deep-reaching fracture structures have been shown to influence the overall ice-shelf dynamics, we propose the fracture-density field introduced here be used as a measure for ice softening and decoupling of the ice flow in fracture-weakened zones. This may yield more accurate and realistic velocity patterns in prognostic simulations. Additionally, the memory of past fracture events links the calving front to the upstream dynamics. Thus the fracture-density field proposed here may be employed in fracture-based calving parameterizations. The aim of this study is to introduce the field and investigate which of the observed surface structures can be reproduced by the simplest physically motivated fracture source terms.

1. INTRODUCTION

Ice shelves are the floating extensions of the large polar ice sheets and are predominantly found around Antarctica. Recent discussion of the rate of global sea-level rise emphasizes the crucial role of ice shelves at the conjunction between atmosphere, ocean and large ice sheets. A shrinkage, or even a loss, of buttressing ice shelves has only a relatively small direct effect on this sea-level rise (Jenkins and Holland, 2007; Shepherd and others, 2010), but it can cause an acceleration and thinning of the upstream tributaries, which increases solid ice discharge from the ice sheet (Rott and others, 2002, 2007, 2011; De Angelis and Skvarca, 2003; Joughin and others, 2004; Rignot and others, 2004, 2008; Scambos and others, 2004; Cook and others, 2005; Rignot, 2006; Bamber and others, 2007; Gudmundsson, 2007; Shepherd and Wingham, 2007; Glasser and Scambos, 2008; Cook and Vaughan, 2010; Joughin and Alley, 2011). Numerical studies are, in principle, able to reproduce this behavior (Schmeltz and others, 2002; Payne and others, 2004; Thomas and others, 2004).

Gravitational driving stresses in ice shelves must be balanced by drag at the lateral shelf margins due to the lack of basal traction. Fractures affect this stress balance by disturbing the ice body's mechanical integrity (e.g. Larour and others, 2004a,b; Vieli and others, 2006, 2007; Khazendar and others, 2009; Humbert and Steinhage, 2011) and thereby reducing the buttressing effect (Dupont and Alley, 2005; Gagliardini and others, 2010). Hence, prognostic ice-sheet models need to incorporate at least the large-scale effects of the complex physics of fracture processes.

Fractures develop from small-scale flaws that have sufficient initial size (Rist and others, 1996, 1999), most likely initiated close to the surface, where the compressive overburden stresses are small. They form in the presence of strong divergence or convergence of the ice flow (Hughes, 1977, 1983) or due to the buckling and shearing close to ice rises and side margins (e.g. Glasser and others, 2009; Cuffey

and Paterson, 2010). Also, the abrupt acceleration and cyclic tidal flexure (e.g. Holdsworth, 1977; Lingle and others, 1981) in the transition zones between grounded or stagnant parts and fast-flowing units of floating ice shelves support fracture formation. As a basic approach, the initiation and growth of large-scale fractures close to the surface, so-called surface crevasses, can be considered in terms of horizontal strain rates or surface stresses. This is a simplification, since, in general, brittle fracture formation is known to depend on the total stress tensor across a crack (Lawn, 1993; Paterson and Wong, 2005). The presence of water strongly influences fracture growth. At the bottom of the ice shelf, crevasses can extend far upward into the ice body, due to sea-water penetration (Weertman, 1980; Jezek and Bentley, 1983; Van der Veen, 1998a; Rist and others, 2002; Luckman and others, 2011). At the surface, meltwater-enhanced fracturing has been proposed as one of the triggers of the catastrophic disintegration of several ice shelves fringing the Antarctic Peninsula in recent decades (Weertman, 1973; Doake and Vaughan, 1991; Rott and others, 1996; Scambos and others, 2000, 2009; MacAyeal and others, 2003; Rack and Rott, 2004; Khazendar and others, 2007; Van der Veen, 2007; Vieli and others, 2007; Glasser and Scambos, 2008; Braun and others, 2009).

Considerable effort has been made to incorporate fracture mechanics into regional diagnostic ice-shelf models: Rist and others (1999), Hulbe and others (2010) and Jansen and others (2010) use a mechanistic two-dimensional (2-D) fracture criterion in diagnostic models to evaluate the stability of the Filchner–Ronne and Larsen C ice shelves, respectively. Humbert and others (2009) identified shear zones and rifts in the Brunt Ice Shelf using observational data and applied additional flow-enhancement factors and a decoupling scheme for the stress balance. Saheicha and others (2006) use the von Mises criterion (Vaughan, 1993), which expresses a relationship between tensile strength and effective stress. The macroscopic effect of fracture structures on the ice body of the Filchner–Ronne Ice Shelf (FRIS) in the diagnostic model is parameterized by softening and decoupling, in order to

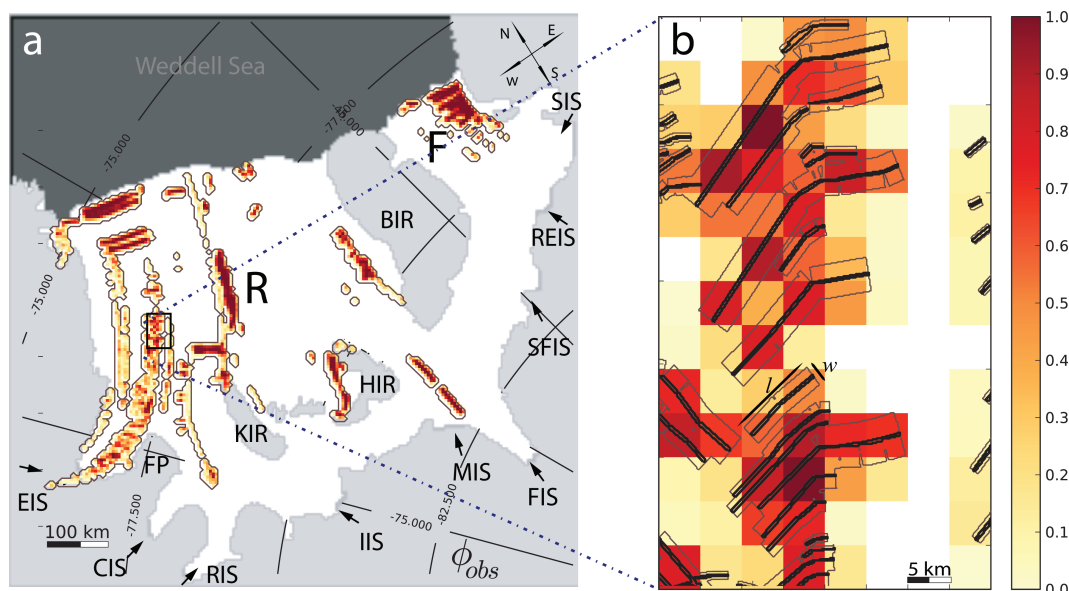


Fig. 1. (a) Observed fracture density, ϕ_{obs} , in the Filchner–Ronne Ice Shelf based on data of Hulbe and others (2010) and Eqn (2) with length-dependent width of the zone of influence, bounded by $1 \text{ km} < w = l/4 < 10 \text{ km}$. Regions of vanishing fracture density are masked. Thin black and gray-dotted lines show the position of the grounding line and observed stream lines. (b) Close-up view of observed fracture density, ϕ_{obs} , overlaid by observed fractures (black) with associate zone of influence (gray contours). Main inlets and ice rises are denoted by abbreviations: R – Ronne Ice Shelf; F – Filchner Ice Shelf; EIS – Evans Ice Stream; CIS – Carlson Inlet; RIS – Rutford Ice Stream; IIS – Institute Ice Stream; MIS – Möller Ice Stream; FIS – Foundation Ice Stream; SFIS – Support Force Ice Stream; REIS – Recovery Ice Stream; SIS – Slessor Ice Stream; FP – Foin Point; KIR – Korff Ice Rise; HIR – Henry Ice Rise; BIR – Berkner Ice Rise.

reproduce characteristic features of the observed velocity distribution. These models identify regions of potential crack opening for given boundary conditions and evaluate their effects on the stress balance. Sandhäger and others (2005) additionally introduced the advection of a variable with the diagnostic velocity field accounting for a shear-zone depth ratio healed with a constant rate.

In order to represent the manifold physical role of fractures on large-scale ice-sheet dynamics we need a well-defined time-evolving field, which is advected with the ice flow. Here we introduce this field as a measure for fracture density and introduce first-order parameterizations for the relevant contributing processes, such as the initiation, growth or healing of fractures. The respective importance of these processes and parameters is evaluated in a suite of numerical experiments. Characteristics of fracture density along the flowline and in side shear regions are discussed for two idealized ice-shelf geometries. The individual pattern of fracture density for realistic scenarios, such as for the large FRIS or the smaller Larsen A+B ice shelf (LABIS) is compared with a snapshot of observed locations of surface features in these ice shelves.

2. FRACTURE-DENSITY FIELD

We define a 2-D field, ϕ , over the entire ice-shelf region, which quantifies the mean area density of fractured ice. The unitless, scalar field variable, ϕ , is bounded by

$$0 \leq \phi \leq 1, \quad (1)$$

where $\phi = 0$ corresponds to non-fractured ice. In observed ice-shelf fracture fields the fracture density, ϕ_{obs} , is defined as the fraction of failed ice, i.e. ice that cannot be described appropriately by an ice-continuity condition (e.g. the Stokes equation). Thus, ϕ_{obs} increases with the number, N , and the length, l , of growing crevasses. Crevasses are discontinuities,

which alter the local stress field within a zone of influence. For comparison with observational fields we assume that the area of failed ice around crevasses is rectangular, spanning a region of horizontal distance w around an individual crevasse. Groups of individual zones of influence can be quantified as a fraction of an ice-shelf surface section as

$$\phi_{\text{obs}} = \frac{Nwl}{\Delta x \Delta y}, \quad (2)$$

where Nw and l are limited to the extent of the discrete mesh, Δx and Δy . For $\phi_{\text{obs}} = 1$ the zone of influence covers the entire discrete gridcell surface (e.g. Fig. 1b).

We consider here macroscopic structural glaciological fracture features, growing from the surface both vertically and horizontally, or closing in appropriate stress regimes. Although the vertical dimension of penetrating crevasses is an essential issue in the discussion of ice-shelf stability, it is not explicitly included in our definition. Instead we focus here on the location of surface crevasses, often collocated in band structures, revealing a depth-dependent density of crevasses. However, ϕ can be expanded to three dimensions, which will be the focus of future studies. In addition, here we do not take into account previous microscale stages of fracture formation, such as subcritical crack growth or damage accumulation (Weiss, 2004; Pralong and Funk, 2005). Such processes depend on the prevailing local stress and produce the flaws necessary to initiate crevasse opening, mostly in firm layers with distinct mechanical properties. Such flaws can hardly be detected at the ice-shelf surface, and do not contribute directly to the fracture density defined here. However, they do play an important indirect role for the fracture-density field, ϕ , by serving as starter cracks, from which the crevasses are initiated. In order to focus on the macroscopic dynamics of fracture growth, we assume a spatially homogeneous field of microcracks.

The fracture density, ϕ , is assumed to be isotropic and it is transported by horizontal advection with the vertically averaged velocity, \mathbf{v} , calculated from the continuum mechanics stress balance in the shallow-shelf approximation (SSA) implemented in the Potsdam Parallel Ice Sheet Model, PISM-PIK (see Appendix for a brief description and Winkelmann and others (2011) for further details) as

$$\frac{\partial \phi}{\partial t} + \mathbf{v} \cdot \nabla \phi = f_s + f_h = f(\dot{\epsilon}, \sigma, \phi, \dots), \quad (3)$$

with forcing term f as the sum of sources, f_s , and healing terms, f_h , which depend on a number of glaciological parameters. To leading order we assume here a sole dependence on the strain rate, $\dot{\epsilon}$, stress, σ , and the fracture density, ϕ , itself. For the source term we write

$$f_s = \psi \cdot (1 - \phi), \quad (4)$$

where ψ is the fracture growth rate. The second factor reduces the source by $(1 - \phi)$ and represents the fracture interaction, bounding the resulting macroscopic fracture density below the threshold, 1. The justification for this term is that the local stress field surrounding a single crevasse is relaxed up to a distance of $\sim 3\text{--}4$ crevasse depths (Sassolas and others, 1996). For closely spaced crevasse bands and, hence, for a relatively high fracture density, additional fracture formation and further fracture penetration is hindered accordingly (Smith, 1976; Weertman, 1977).

2.1. Longitudinal spreading as source of fracture growth

Ice shelves spread under their own weight at a rate that is generally high in the vicinity of the grounding line, where it goes afloat. In two horizontal dimensions we attempt here a formulation using merely the eigenvalues of the vertically averaged strain-rate tensor, $\dot{\epsilon}_1$ and $\dot{\epsilon}_2$, where $\dot{\epsilon}_1 \geq \dot{\epsilon}_2$. These eigenvalues represent expansion ($\dot{\epsilon}_{1,2} > 0$) or contraction ($\dot{\epsilon}_{1,2} < 0$) along the principal directions. In isotropic ice the initial opening of surface cracks is observed to be transverse to the principal direction of strongest stretching (Holdsworth, 1969; Rist and others, 1999). For the purpose of this study, we use a simple formulation in terms of the maximum spreading rate (not the total effective strain rate) to capture the first-order effect and understand how much of the observed fracture fields can be reproduced by this simple approach. Hence, we formulate the fracture growth rate for the fracture-density source (Eqn (4)) as

$$\psi = \gamma \cdot \dot{\epsilon}_1, \quad (5)$$

where γ is a unitless constant parameter which, in general, should be a function of flow law parameters, such as the temperature-dependent ice softness. For this uniaxial case without healing ($f_h = 0$) we can derive, from Eqns (3–5), an exact analytical steady-state solution, which only depends on the velocity distribution, $u(x)$, along the flowline,

$$\phi(x) = 1 - (1 - \phi_0) \left(u(x)/u_0 \right)^{-\gamma}, \quad (6)$$

and a given inflow velocity, $u_0 = u(x_0)$. The boundary value, $\phi_0 = \phi(x_0)$, is associated with pre-existing cracks which have formed upstream in the tributaries or with crevasses initiated at the grounding line (e.g. due to tidal flexure (Section 2.3)). In the unconfined flowline case, the function $\phi(x)$ is strictly monotonic, since $\dot{\epsilon}_1$ is tensile everywhere, i.e. positive values meaning expansive flow. The parameter γ becomes an exponent here, determining the curvature of the

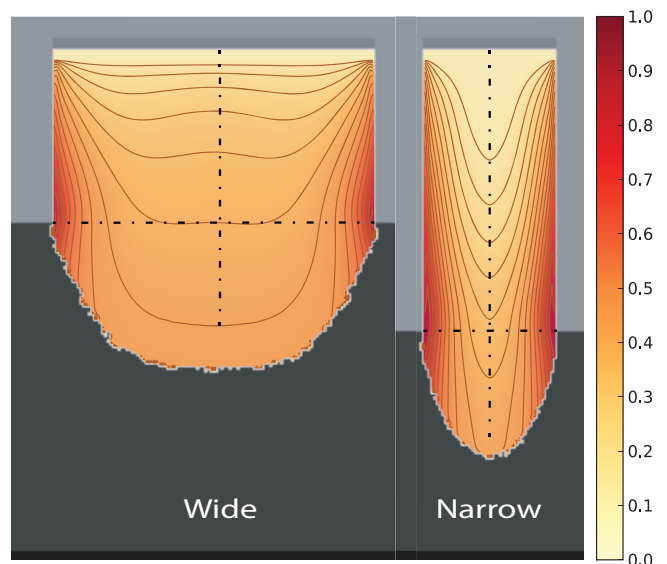


Fig. 2. Steady-state fracture density, ϕ , for an ice shelf confined in a rectangular bay 300 km wide and 150 km long (left) or 150 km wide and 250 km long (right), with constant $\gamma = 0.5$. Ice flows into the bay at the top boundary with $\phi_0 = 0.1$, ice thickness 600 m and maximal speed 300 m a^{-1} . Along the sides, friction is parameterized by a viscosity $\eta_B = 5 \times 10^{13} \text{ Pa s}$. At the ice-shelf front, ice calves off for an ice thickness less than 175 m. Melting and accumulation is neglected. Black dashed lines show lateral and cross sections along which profiles are plotted in Figure 3.

function. The larger γ , the faster ϕ approaches saturation (at $\phi = 1$).

Experiments with idealized ice-shelf geometry

In this first-order formulation we calculate the 2-D steady-state fracture density, $\phi(x, y)$, with PISM-PIK for an ice shelf confined in an idealized rectangular bay with unidirectional inflow (Fig. 2). We chose a parameter value $\gamma = 0.5$ for the fracture growth rate and boundary condition $\phi_0 = 0.1$. The steady-state profiles of ice thickness, H , velocity, u , and hence the larger principal strain rate, $\dot{\epsilon}_1$, along the center line, x , of the wide ice shelf (Fig. 3a) are close to the analytical flowline solution of an unconfined ice shelf spreading in one direction (Van der Veen, 1999; gray dashed curve in Fig. 3a and b) since in the wide geometry the buttressing effect of side drag is small in the inner part. Inserting this analytical velocity solution into Eqn (6) yields the fracture density

$$\phi(x) = 1 - (1 - \phi_0) \left(\frac{4CH_0^3}{u_0} x + 1 \right)^{-\gamma/4}, \quad (7)$$

where $C = [\rho g (\rho_w - \rho) / (4\rho_w B_0)]^3 = 2.45 \times 10^{-18} \text{ m}^{-3} \text{ s}^{-1}$ comprises material constants, such as the ice density, ρ , sea-water density, ρ_w , and the acceleration due to gravity, g , as well as the constant ice stiffness rate factor, B_0 . Even though in the simulations a temperature-dependent ice stiffness, $B = B(T)$, is used, the obtained fracture density along the center line is very close to the analytical solution of Eqn (7) and increases up to a value of 0.4 at the mouth of the embayment. At the side margins, where friction is prescribed by a staggered boundary viscosity, strong shearing yields large magnitudes of both principal strain-rate components, while the minor component, $\dot{\epsilon}_2$, is generally compressive

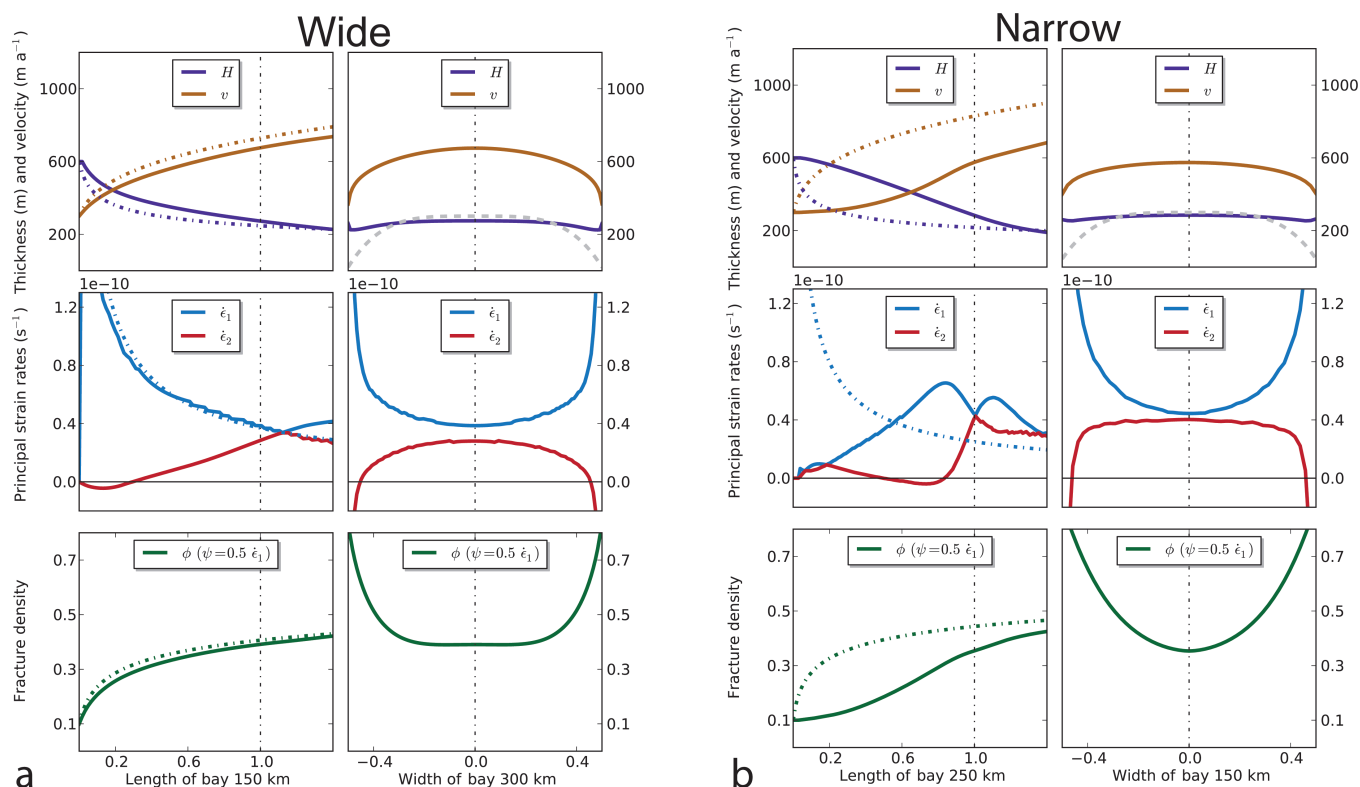


Fig. 3. Obtained velocity, ice thickness, principal horizontal strain rates and the inferred fracture-density field evolution for ice shelves confined in a rectangular bay (a) 300 km wide and 150 km long and (b) 150 km wide and 250 km long (Fig. 2). Profiles are normalized to unity length and width and plotted in lateral view along the center line (left panel columns) and across the mouth of the bay (right panel columns). The black dashed vertical line in the left panel columns shows the position of the mouth of the bay. The gray dashed profile on the upper right panel shows the unidirectional inflow velocity applied at the upstream boundary. Steady-state values in the wide case are close to the analytical solution of an unbuttressed flowline ice shelf plotted as dashed curve, whereas in the narrow case profiles vary strongly. In the lower panels steady-state fracture densities with $\phi_0 = 0.1$ are shown.

here with respect to the principal axes (Nye, 1952). The parameterization presented here leads to steady-state values of the fracture density up to 0.8 close to the side margins (right column, Fig. 3a). Figure 3b shows the profiles of ice thickness and velocity of an ice shelf confined in a comparably narrow bay, 150 km wide and 250 km long. For the same lateral friction as for the wide-bay set-up we find a strong buttressing effect also in the inner part of the ice shelf, indicated by much thicker and slower ice compared to the less confined, i.e. wider, case. This leads to smaller spreading rates in the upstream region and hence to a smaller fracture density there. When the ice shelf leaves the narrow bay it can extend freely, which leads to maximal spreading rates, up to $\dot{\epsilon}_1 = 7 \times 10^{-11} \text{ s}^{-1}$, and hence to a strong increase in fracture density close to the value of the wide ice shelf at this position. Accordingly, the profiles across the mouth of the narrow bay are similar to the results of the wide bay (compare right columns of Fig. 3a and b).

Experiments with a realistic ice-shelf geometry

In a realistic set-up, such as for the FRIS, the resulting fracture-density field can be phenomenologically compared with observations, i.e. the location of areas with many surface features for a certain snapshot can be compared with features of the obtained fracture-density pattern, indicated by comparably high values. In contrast to the simulations with an idealized geometry (Fig. 2) we prescribe the ice thickness in the simulations with realistic topography and specify boundary conditions (see Section 2.2 and Appendix

for precise values). This is necessary in order to avoid significant errors from a dynamic calculation of the flow field. We simulate the evolution of fracture density starting from an initial zero state in the whole ice-shelf domain. After reaching a steady state, fracture density is highest in the stagnant outer shear regions and downstream of regions that have been subject to shearing along the side margins or promontories (Fig. 4a). Separate flow units draining from different inlets can be identified in the structure, but the steady-state pattern of the fracture field appears comparably smooth. While the locations of some features compare well with observations, pronounced bands of observed surface features, as evaluated by Hulbe and others (2010) from Moderate Resolution Imaging Spectroradiometer (MODIS) Mosaic of Antarctica (MOA) image maps, can hardly be identified in the fracture-density pattern. Fracture density is also high in areas where the flow is comparably slow, such as upstream of ice rises. Since, in reality, fractures are not expected to form in those low-strain-rate areas, this suggests the introduction of a critical threshold for fracture initiation. Observations suggest physically reasonable thresholds for crevasse initiation defined in terms of stresses, i.e. at high effective stresses (e.g. Vaughan, 1993). Below these thresholds fractures may close and heal due to the overburden pressure, accumulation or refreezing.

2.2. Crevasse initiation threshold

Observed crevasse bands downstream of inlet corners, converging streams and ice rises aligned in the flow direction

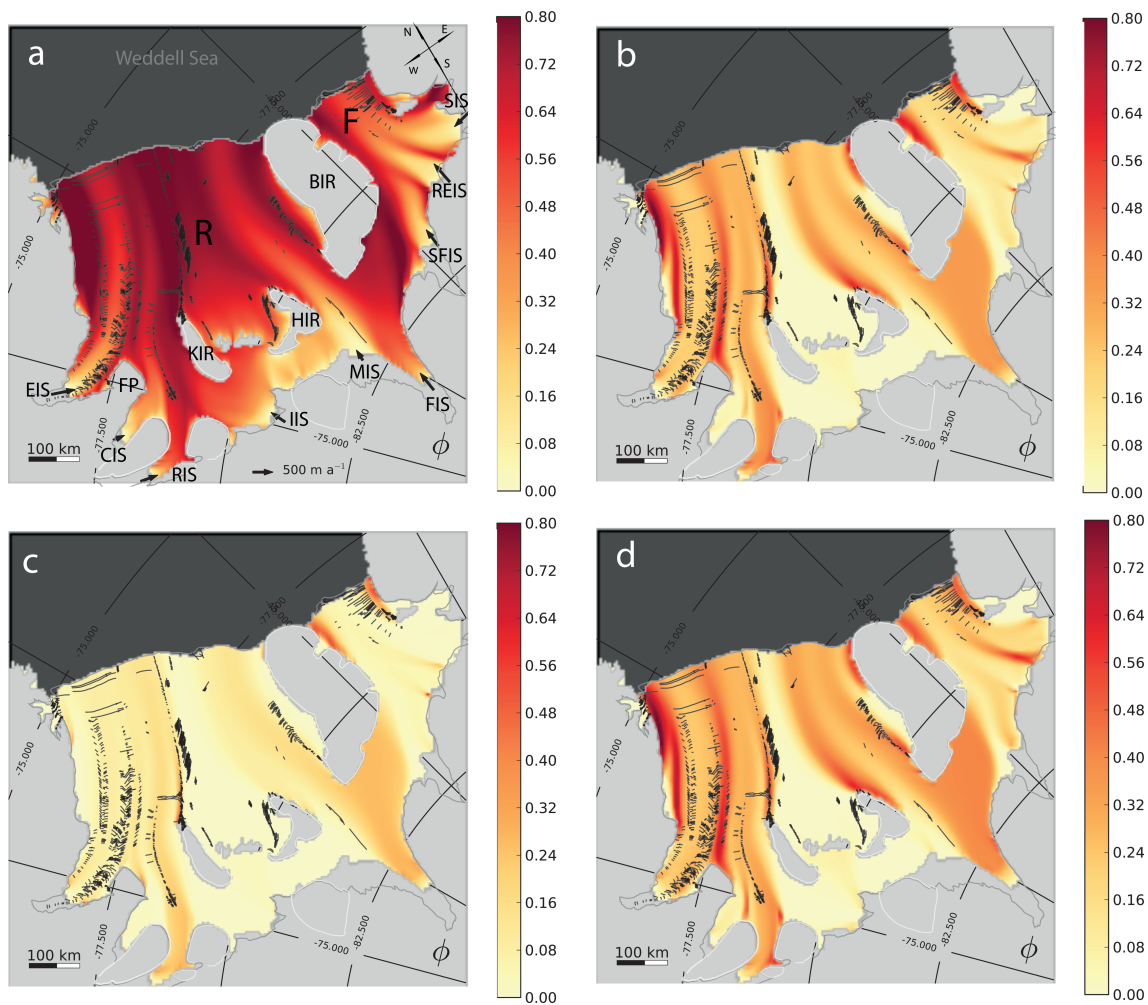


Fig. 4. Steady-state distribution of the fracture density in a realistic set-up of the FRIS for varying fracture initiation thresholds, σ_{cr} : (a) 0 kPa, (b, d) 70 kPa and (c) 90 kPa in von Mises fracture criterion with fracture growth parameter $\gamma = 0.3$, and without contribution through the inlets, $\phi_0 = 0$. Results shown in (d) are obtained by choosing a fracture growth rate with a constant $\psi = \gamma \bar{\epsilon}_1$. For a fixed ice thickness, a flow enhancement of $E_{SSA} = 0.4$ and with parameterized side friction by $\eta_B = 10^{15}$ Pa s, the fracture density is transported with a steady SSA velocity field. Overlaid, observed visible surface fractures, kindly provided by Hulbe and others (2010, fig. 1).

suggest an initiation of fractures in the intense shearing regions once a certain threshold is reached. Based mainly on laboratory experiments, these critical values are often defined in terms of effective stress or similar rotational invariant flow properties, such as combinations of stress or strain-rate eigenvalues. Fracture initiation starts from the surface, where the overburden pressure vanishes. The mechanical properties of the upper firn layer are distinct, but strain rates are mostly constant with depth (Nath and Vaughan, 2003). A variety of phenomenological criteria, such as the von Mises criterion (Vaughan, 1993), the Coulomb criterion or even advanced mixed-mode crevassing with maximum circumferential stress criterion based on linear-elastic fracture mechanics (e.g. Kenneally and Hughes, 2006), can identify regions where creep failure and fracture initiation most likely occur.

We choose the simple von Mises criterion, which is based on the so-called ‘maximum octahedral shear stress’, defined in terms of surface-parallel principal stresses, σ_+ and σ_- , as

$$\sigma_t = \sqrt{\sigma_+^2 + \sigma_-^2 - \sigma_+ \sigma_-} \quad (8)$$

The range of literature values of the tensile strength, σ_t , that ice can support is 90–320 kPa (Vaughan, 1993). This

large range may be due to the uncertainty in stress/strain-rate conversion of observational data with the constitutive flow law, as well as to the effects of temperature, density and firn structure. Tensile strengths in Antarctic ice shelves are found around the median of this literature range. On the basis of the von Mises criterion we refine our fracture growth rate (Eqn (5)) to

$$\dot{f}_s = \gamma \cdot \dot{\epsilon}_1 \cdot (1 - \phi) \cdot \Theta(\sigma_t - \sigma_{cr}), \quad (9)$$

where the additional $\Theta(\Delta)$ is the Heaviside step function to predict regions of potential fracture growth, defined as

$$\Theta(\Delta) = \begin{cases} 1, & \Delta > 0 \\ 0, & \Delta \leq 0. \end{cases} \quad (10)$$

In the following we discuss the effect of this critical value on the steady-state fracture-density pattern in a model of the FRIS. In order to be close to observed conditions, ice thickness and all other boundary conditions are prescribed and the three-dimensional (3-D) temperature evolution has already reached an equilibrium state close to observations. Some parameter must be determined to achieve the most realistic flow pattern for the given model configuration.

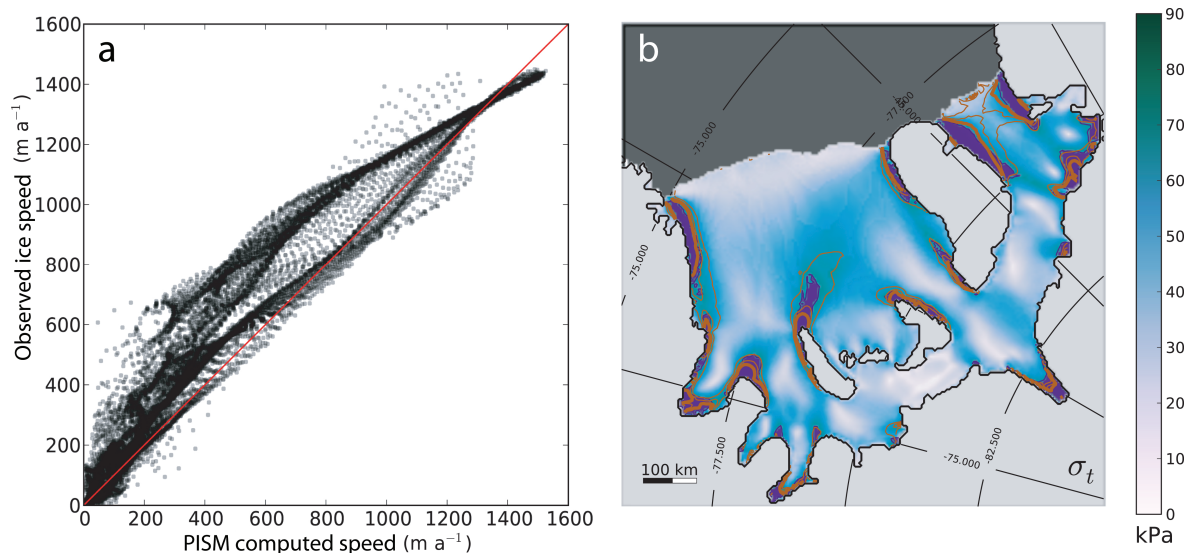


Fig. 5. (a) Scatter plot showing a comparison of calculated vs observed surface speed values within the ice-shelf domain for an optimal parameter configuration of $E_{SSA} = 0.4$ and $\eta_B = 10^{15}$ Pa s. (b) Distribution of calculated von Mises effective stress, σ_t , in the FRIS. Values larger than critical effective stress, $\sigma_{cr} = 70$ kPa, colored in purple, are found in confined shear regions at the inlets and some side margins and where flow units merge. A maximum spreading rate of $\sim \bar{\epsilon}_1 > 2.5 \times 10^{-10} \text{ s}^{-1}$ is obtained in most parts of the indicated regions (thick brown contours). Thin brown contours delineate lower spreading rate, i.e. 1.5 and $2.0 \times 10^{-10} \text{ s}^{-1}$.

The lateral friction of the ice shelf, parameterized by the boundary viscosity, η_B , strongly influences the strain-rate and stress fields, and thereby the fracture-density field. Higher friction leads to vanishing ice speed along the margins and to strong shearing, but also to much slower speeds in the interior and outer parts of the ice shelf, which can be compensated by a larger enhancement factor. Comparison with reconstructed observational ice surface speed data (especially for lower speeds) suggests the use of a comparably small side friction (Fig. 5a). It was set to $\eta_B = 10^{15}$ Pa s. This accounts for the partial decoupling of large interior flow units from the sides along weak zones. As long as this feature is not captured in the flow model (Section 3), a suitable enhancement factor for the SSA calculation has to be chosen. Such an enhancement factor is generally used to account for anisotropy and grain-size effects in the ice shelf (Ma and others, 2010). Hence, the vertically averaged effective viscosity in the SSA-stress balance scales with $E_{SSA}^{-1/n}$ (Winkelmann and others, 2011, their eqn (10)). Best comparison with observations in the FRIS with a root-mean-square deviation of the velocity vector components of only 108 m a^{-1} averaged over $\sim 14\,000$ points and a cross-correlation coefficient $r^2 = 0.96$ is achieved with a relatively low value of $E_{SSA} = 0.4$.

The steady effective stresses inferred in this way are comparably low, and regions of likely creep failure identified with the von Mises criterion with a threshold below the literature range (e.g. $\sigma_{cr} = 70$ kPa) cover only 4% of the total FRIS area, indicated by purple shaded areas in Figure 5b. These shear regions are found at the major inlets, downstream of ice rises at flow unit junctions, but also at shearing margins, particularly in the narrow Filchner Ice Shelf. Thus, fractures grow according to the corresponding spreading rate, which is, on average, $\sim \bar{\epsilon}_1 = 3 \times 10^{-10} \text{ s}^{-1}$ in those regions. In observations much higher strain rates are found in the confined suture zones and at shear margins. A softening of ice in areas of high fracture density would account for this effect (Section 3).

The modeled fracture-density value is associated with the frequency, length and width of the zone of influence of fractures, but a precise quantitative validation can only be made on the basis of widespread ice-penetrating radar data. In our basic formulation we have to choose a somewhat arbitrary value for parameter γ , so the resultant fracture density produces a physically meaningful steady-state pattern, reflecting relevant features of observed surface structures (Fig. 4b–d). Maximum calculated fracture-density values peak around $\phi_{max} = 0.8$, particularly in the outer shear regions close to the front. In those regions the fracture interaction factor, $(1 - \phi)$, has a significant effect, which is expected in the dynamics of real crevasse trains.

For increasing fracture initiation threshold, σ_{cr} , we find more-pronounced band structures downstream of ice rises and prominent geographical features, which agrees with the location of crevasse trains in observations (compare Fig. 4a and b). For even higher threshold values (within the range of the literature values) some of the features are no longer reproduced (e.g. fractures in the suture zone of the merging flow units of Evans and Rutford Ice Streams (EIS and RIS) in Fig. 4c). Most relevant features of the observational data map are best represented for a threshold of $\sigma_{cr} = 70$ kPa (Fig. 4b). The reddish bands (high fracture density) coincide very well with observed fracture bands and streak lines (except for those structures formed at ice rumples, that are not considered in our model, such as Kershaw ice rumples between FP and KIR). If we choose a length-dependent width, $w = l/4 < 10$ km, for the zone of influence around an observed crevasse, we can compute an observed fracture density snapshot, ϕ_{obs} on the 5 km grid (Eqn (2)). Figure 1 shows the resulting bands of high crevasse density aligned in the flow direction and in shear regions, which can be compared to the obtained smooth model fracture density, ϕ (e.g. Fig. 4). The close-up view in Figure 1 reveals the spatially varying distribution of ϕ_{obs} . A time average over several snapshots of sufficient delay would give a much smoother distribution. The width, w , scales the observed

fracture density as long as the overlap of individual zones of influence is small. In any case, comparison of the model's fracture field can only be complete if the area of failed ice can be determined from observations, since the geometrical derivation proposed here for surface crevasses is merely a rough approximation of the quantity that we proposed as the fracture field, ϕ . Large rifts observed close to the calving front are apparently not captured by the model ϕ . Since no healing is applied so far, the steady-state fracture density can also accumulate in very slow-moving sections, such as upstream of Berkner Ice Rise (BIR) supplied by the contributions of the Rutford and Foundation Ice Streams (RIS and FIS).

Regarding the effects of fracture initiation, $\Theta(\sigma_t - \sigma_{cr})$, and fracture growth rate, $\psi = \gamma \dot{\epsilon}_1$, the resulting steady-state fracture-density pattern is apparently more sensitive to the fracture initiation threshold than to the growth rate. If we replace the spreading rate by its mean value found in the initiation regions, i.e. $\sim \bar{\dot{\epsilon}}_1 = 3 \times 10^{-10} \text{ s}^{-1}$, we get a similar pattern (compare Fig. 4b and d).

Rist and others (1999, plate 1) provide a map of the FRIS crevasse pattern using visible and radar imagery. Most of the fracture features coincide with the map inferred by Hulbe and others (2010), except for fracture fields in the central Ronne Ice Shelf downstream of Korff and Henry Ice Rises (KIR and HIR), probably ice with densely distributed short and inactive fractures covered with snow and not seen in visual inspection of MODIS images nor in the obtained fracture-density field.

In a simulation of the northern Larsen Ice Shelf (A+B) we use the same flow parameters as in the FRIS, which yields a velocity field that differs from observed velocities with a cross-correlation coefficient of $r^2 = 0.78$. A varying combination of flow enhancement and friction parameter does not much improve this result. A fracture-density dependent rheology may correct for this underestimation of velocities, as in many other smaller buttressing ice shelves. Nevertheless, the evolution of the fracture density with parameters $\sigma_{cr} = 70 \text{ kPa}$ and $\gamma = 0.5$ produces a pattern (Fig. 6) which compares well with the advanced satellite image interpretations of Glasser and Scambos (2008, fig. 4). Elongated steady-state bands initiated at the inlet corners of the main tributaries following the ice flow down to the ice-shelf front agree with crevasse patterns in the images (at inlet corners even rifts are formed). Similar longitudinal structures in observations separate transversally the stagnant regions around the Seal Nunataks (SNI), Cape Disappointment (CD), Jason Peninsula (JP) and Foyon Point (FP) from the faster-flowing interior units.

2.3. Contributing tributaries

An important contribution to the observed elongated surface structures originates from the transition zone in the vicinity of the grounding line (tensile modes) and at inlet corners (shear modes) of the tributary glaciers. In the ice-shelf region supplied by EIS, trains of deep crevasses are found all the way up to the grounding line (Hulbe and others, 2010). Such structures are created in localized high shear rate regions through interaction with bedrock features (Glasser and Scambos, 2008). Since we discuss only the dynamics of floating ice shelves, without the complex transition zone processes, pre-existing fractures along tributary inlet glaciers can be treated here only as a boundary condition, ϕ_0 , for the fracture-density field. We choose arbitrary constant values here for the upstream contribution, since it is beyond

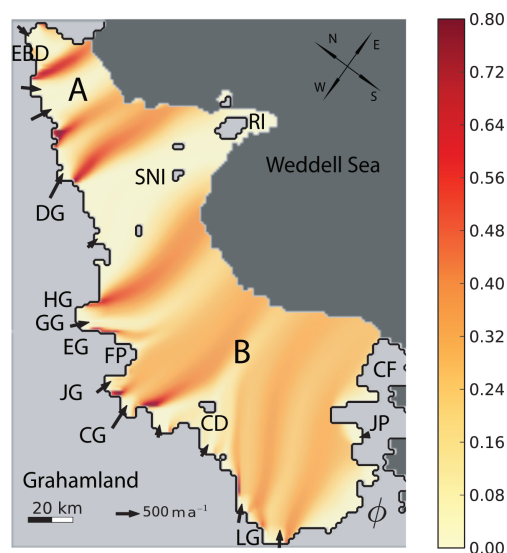


Fig. 6. Steady-state distribution of the fracture-density field for $\gamma = 0.5$, $\phi_0 = 0$ and $\sigma_{cr} = 70 \text{ kPa}$ for a fixed geometry of the Larsen A+B ice shelf with a steady SSA velocity field. RI – Robertson Island; SNI – Seal Nunataks; CD – Cape Disappointment; CF – Cape Framnes; JP – Jason Peninsula; LG – Leppard Glacier; CG – Crane Glacier; JG – Jorum Glacier; FP – Foyon Point; EG – Evans Glacier; GG – Green Glacier; HG – Hektor Glacier; DG – Drygalski Glacier; EBD – Edgeworth Bombareier and Dinsmoor Glaciers.

the scope of this study to investigate fracture initiation and growth of grounded ice. Figure 7a shows how the boundary fracture density of $\phi_0 = 0.4$ affects the overall steady-state distribution. Basically, the pronounced band structure remains unchanged (cf. Fig. 4b) while the fracture-density value is increased in a smooth way in areas between those bands. Note that in the wake of the ice rises HIR and KIR, in the interior of Ronne Ice Shelf, the fracture density is very low. Low strain rates yield weak fracture initiation and growth in this region. At the same time this area is shielded from the inflow of inlet fractures by the ice rises.

2.4. Healing and persistence of crevasses

Healing processes may close existing crevasses or generally transform weak and fractured ice to harder and compact ice. Studies concerning the dynamics of ice healing are rare. To our knowledge, none provides a quantitative or observational characterization of such processes. Pralong and Funk (2005) assumed, to a first approximation, that healing follows the dynamics of crack growth, i.e. it can be expressed as a sink term in the fracture density evolution equation. We write

$$\dot{f}_h = \Theta(-\psi_h) \cdot \psi_h, \quad \text{with} \quad \psi_h = \gamma_h (\dot{\epsilon}_1 - \dot{\epsilon}_h). \quad (11)$$

This expression is similar to the source in Eqn (4), but contributes only negative ψ_h , i.e. below a certain threshold. Hence, ψ_h represents a healing rate, which is more effective the smaller the spreading rate is compared to a certain upper spreading rate threshold, $\dot{\epsilon}_h$. This formulation is a simple representation of the closure effect due to the ice overburden pressure. For deep rifts or bottom crevasses, it has been suggested that refreezing and basal healing by marine ice along suture bands and in the wake of promontories and islands also play important roles as healing processes (Glasser and others, 2009; Holland and others, 2009; Hulbe

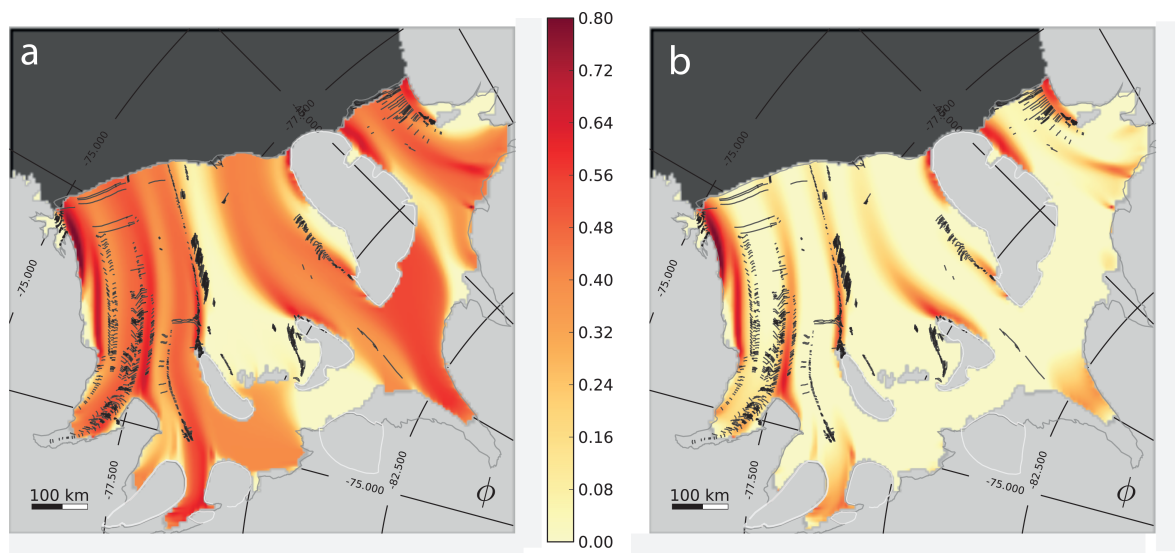


Fig. 7. Steady-state fracture density for Filchner–Ronne simulation with (a) fracture density boundary condition for the inlets $\phi_0 = 0.4$ and (b) healing rate, $\gamma_h = 0.1$, and $\psi_h = \dot{\epsilon}_1 - 2 \times 10^{-10} \text{ s}^{-1}$, but with $\phi_0 = 0$. Parameters for fracture initiation are chosen as $\sigma_{cr} = 70 \text{ kPa}$ and $\gamma = 0.3$ (cf. Fig. 4b).

and others, 2010). Since quantitative measurements, which would allow a better parameterization of large-scale healing, are not yet available we here neglect the dependence of healing on the local fracture density. Figure 7b shows the steady-state fracture density with healing parameters of $\dot{\epsilon}_h = 2.0 \times 10^{-10} \text{ s}^{-1}$ and $\gamma_h = 0.1$. Contributions of the inlets to the fracture density vanish on the way downstream, while along the shear zones the healing effect is negligible. As healing acts in slowly moving sections over a prolonged time interval, e.g. upstream of Berkner Ice Rise (BIR), supplied by the contributions of the Rutford and Foundation Ice Streams (RIS and FIS), fracture density vanishes completely. The numerical first-order explicit upwind scheme used for transport of the fracture density implemented in PISM-PIK causes an artificial diffusion, which causes the fading of band structures downstream of fracture formation areas and represents numerical unintended healing.

Observed longitudinal surface features can form far upstream, where fast-flowing glaciers begin, and persist over long distances downstream (sometimes all the way to the calving front). Considering the critical values for healing and fracture initiation, we can identify regions of intermediate stresses, where $\dot{\epsilon}_1 > \dot{\epsilon}_h$ and $\sigma_t < \sigma_{cr}$ is valid and fracture density stays more-or-less constant. In reality, sufficient large crevasses are observed to grow for strain rates below the initiation thresholds (Rist and others, 1999), which should be expressed by $\sigma_{cr} = \sigma_{cr}(\phi)$. Temperature also plays an important role here, since brittle failure processes favor colder and stiffer ice, which is particularly relevant for cold ice draining through the inlets from the upstream high-altitude catchments. Weiss (2004) introduced a concept of subcritical crack growth for stress values below the fracture formation threshold range given by Vaughan (1993). Depending on the changing stress history, while moving with the ice these flaws may grow at comparably low rates and precondition accelerated unstable crack growth further downstream in later stages of failure. An alternative approach to describe the formation of such cracks in isotropic polycrystalline materials has been proposed in

terms of linear-elastic fracture mechanics in combination with dislocation theory (e.g. Griffiths, 1921; Weertman, 1996; Van der Veen, 1998b; Kenneally and Hughes, 2002, 2004, 2006). This approach will not be considered further here, but could be implemented in terms of a fracture initiation function replacing $\Theta(\Delta\sigma)$.

3. CONCLUSIONS AND PROSPECTS

We introduce a macroscopic fracture-density field in ice shelves within the framework of an ordinary continuum flow model in the shallow approximation. In doing so, we take a minimalistic approach, in the sense that we aim to investigate which of the observed ice fractures can be reproduced by first-order fracture initiation, fracture growth and healing terms. The fracture density in the applied simple formulation in terms of strain rates and effective stresses yields a map of pronounced zones of high values separating flow units of lower density values, which qualitatively agrees with the pattern of surface fractures in satellite-visible imagery. Extensive deep-reaching radar observations in fracturing ice-shelf areas could provide the means for an actual quantitative relationship in terms of depth, length and distance between fractures per area and for a more general power-law formulation of source or healing terms with additional parameters distinguishing between fracture-related processes in different flow regimes in a more process-oriented physical way. The aim here is to introduce a practical way to incorporate fracture into large-scale ice-shelf modeling, that can be eventually expanded to ice streams and ice sheets. Therefore only first-order terms are used. In future studies it is proposed to implement the fracture density for the mechanical decoupling of adjacent flow regions along areas in which the continuum assumption fails and additionally to use it in calving parameterizations at the ice margins.

The implementation of active fracture-induced softening as a dynamic feedback is proposed as an improvement towards more-realistic flow behavior. The inferred location and level

of fracturing provides the relevant information to capture its first-order macroscopic imprint on the main flow regime, by modification of the ice rheology at these positions, in order to achieve more accurate flow simulations. Skrzypek and Ganczarski (1999), Pralong and Funk (2005) and Pralong and others (2006) suggest using the constitutive equation formalism of the continuous non-fractured material to apply a fracture-density dependent softness rate factor in weak fracture zones with regard to the equivalence principle.

Additionally, decoupling schemes as internal boundary conditions are needed to capture the partly mechanical separation of the flow dynamics of adjacent ice-shelf units. Time-dependent property changes in the evolution of zones of weak ice could be considered, such as meltwater-induced hydro-fracturing at the surface (Glasser and Scambos, 2008). It is suggested that effects of reduced marine ice formation (Holland and others, 2009) and sea-water enhanced bottom cracking in suture zones play an additional important role in the preconditioning of rapid collapse events in the style of the Larsen B ice shelf in 2002. Our approach could be expanded to the simulation of fast-flowing ice streams, to capture the manifold observed mechanical decoupling from the side margins and hence a possibly stronger response of the plug-like flow to perturbations. Hence, flow simulations capturing fracture dynamics give a more reliable picture of the vulnerability of, particularly, the smaller ice shelves facing a warming climate.

A second possible application of the fracture-density field is large-scale calving. The calving-front position with respect to the confining coast geometry affects the overall ice dynamics (Hughes, 1983; Dupont and Alley, 2005, 2006). Most calving processes are initiated by tensile crevasse formation, when surface and bottom fractures penetrate a significant portion of the ice thickness (Reeh, 1968; Hughes, 1989). If the ice shelf spreads beyond its anchoring confinements the flow regime changes structurally (Doake, 2001), as transversal spreading occurs at a rate that may exceed the longitudinal spreading (definition $\dot{\epsilon}_2 \leq \dot{\epsilon}_1$ is still valid; see also Fig. 3) and tensile cracks may open and widen in two directions of the principal axes in the vicinity of the central front (Nye, 1952; Hambrey and Müller, 1978). Fractures are observed to grow and become deep crevasses parallel and perpendicular to the calving front, which can even penetrate the whole ice thickness influenced by weak zones (Hulbe and others, 2010). Along intersecting rifts tabular icebergs are finally released (Rist and others, 2002; Larour and others, 2004a; Joughin and MacAyeal, 2005; Hammann and Sandhäger, 2006; Kenneally and Hughes, 2006). In this purely expansive region we define $\dot{\epsilon}_{1,2} > 0$ as the condition to identify the ice-shelf region promoting unstable rift growth and supporting calving. In a first-order approach by Levermann and others (2011), as a 2-D model-applicable extension of the observational relationship inferred by Alley and others (2008), the average calving rate at the front, c , is parameterized by the product of the two strain-rate eigenvalues, which represents the calving kinematics, multiplied by a constant, k , which comprises all material properties. In this form the calving law has already been used in simulations of the Antarctic ice sheet forced with present-day boundary conditions (Martin and others, 2011), as well as in higher-resolution simulations of the Larsen and Ross Ice Shelves. This 'eigencalving' parameterization, however, only represents the kinematic first-order contribution to calving. It needs

to be complemented by the material properties of the ice. This can be achieved through the fracture-density field by introduction of a proportionality constant, k_ϕ , which depends on the fracture-density field and thereby incorporates the material properties of the ice to first order:

$$c \equiv k_\phi \dot{\epsilon}_1 \dot{\epsilon}_2 \quad \text{and} \quad \dot{\epsilon}_{1,2} > 0, \quad (12)$$

with k_ϕ (m s) evaluated at the calving front. Such a calving law cannot predict individual intermittent calving events (Bassis, 2011), but it links average calving probability at the terminus to ice dynamics in the entire ice region and motivates the idea of the fracture-density field discussed in this paper. Fracture penetration depth plays an important role in the precondition of calving and will be considered in a 3-D extension of the fracture-density definition. The implementation of such continuous calving rates in finite-difference schemes requires a subgrid representation of the calving front, as introduced by Albrecht and others (2011). Thus the fracture-density field introduced here is meant to serve as a practical tool to incorporate first-order effects of ice fracturing into large-scale ice modeling.

ACKNOWLEDGEMENTS

We thank Ed Bueler and Constantine Khroulev for providing the sophisticated model base code and plentiful advice, and Maria A. Martin and Ricarda Winkelmann for a critical discussion of the study. We are very grateful to Doug MacAyeal for helpful comments and suggestions. The data of observed surface features on the FRIS were kindly provided by Christina L. Hulbe and Christine LeDoux. T.A. is funded by the German National Academic Foundation (Studienstiftung des deutschen Volkes).

REFERENCES

- Albrecht T, Martin M, Haseloff M, Winkelmann R and Levermann A (2011) Parameterization for subgrid-scale motion of ice-shelf calving-fronts. *Cryosphere*, **5**(1), 35–44
- Alley RB and 7 others (2008) A simple law for ice-shelf calving. *Science*, **322**(5906), 1344
- Balay S and 8 others (2008) *PETSc user's manual*. Argonne National Laboratory, Argonne, IL
- Bamber JL, Alley RB and Joughin I (2007) Rapid response of modern day ice sheets to external forcing. *Earth Planet. Sci. Lett.*, **257**(1–2), 1–13
- Bassis JN (2011) The statistical physics of iceberg calving and the emergence of universal calving laws. *J. Glaciol.*, **57**(201), 3–16
- Braun M, Humbert A and Moll A (2009) Changes of Wilkins Ice Shelf over the past 15 years and inferences on its stability. *Cryosphere*, **3**(1), 41–56
- Bueler E and Brown J (2009) Shallow shelf approximation as a 'sliding law' in a thermomechanically coupled ice sheet model. *J. Geophys. Res.*, **114**(F3), F03008 (doi: 10.1029/2008JF001179)
- Comiso JC (2000) Variability and trends in Antarctic surface temperatures from in situ and satellite infrared measurements. *J. Climate*, **13**(10), 1674–1696
- Cook AJ and Vaughan DG (2010) Overview of areal changes of the ice shelves on the Antarctic Peninsula over the past 50 years. *Cryosphere*, **4**(1), 77–98
- Cook AJ, Fox AJ, Vaughan DG and Ferrigno JG (2005) Retreating glacier fronts on the Antarctic Peninsula over the past half-century. *Science*, **308**(5721), 541–544
- Cuffey KM and Paterson WSB (2010) *The physics of glaciers*, 4th edn. Butterworth-Heinemann, Oxford

- De Angelis H and Skvarca P (2003) Glacier surge after ice shelf collapse. *Science*, **299**(5612), 1560–1562
- Doake CSM (2001) Ice-shelf stability. In Steele J, Thorpe S and Turekian K eds. *Encyclopedia of ocean sciences*. Academic Press, San Diego, CA, 1282–1290
- Doake CSM and Vaughan DG (1991) Rapid disintegration of the Wordie Ice Shelf in response to atmospheric warming. *Nature*, **350**(6316), 328–330
- Dupont TK and Alley RB (2005) Assessment of the importance of ice-shelf buttressing to ice-sheet flow. *Geophys. Res. Lett.*, **32**(4), L04503 (doi: 10.1029/2004GL020224)
- Dupont TK and Alley RB (2006) Role of small ice shelves in sea-level rise. *Geophys. Res. Lett.*, **33**(9), L09503 (doi: 10.1029/2005GL025665)
- Gagliardini O, Durand G, Zwinger T, Hindmarsh RCA and Le Meur E (2010) Coupling of ice-shelf melting and buttressing is a key process in ice-sheets dynamics. *Geophys. Res. Lett.*, **37**(14), L14501 (doi: 10.1029/2010GL043334)
- Glasser NF and Scambos TA (2008) A structural glaciological analysis of the 2002 Larsen B ice-shelf collapse. *J. Glaciol.*, **54**(184), 3–16
- Glasser N and 7 others (2009) Surface structure and stability of the Larsen C ice shelf, Antarctic Peninsula. *J. Glaciol.*, **55**(191), 400–410
- Griffiths AA (1921) The phenomena of rupture and flow in solids. *Philos. Trans. R. Soc. London, Ser. A*, **221**(582–593), 163–198
- Gudmundsson GH (2007) Tides and the flow of Rutford Ice Stream, West Antarctica. *J. Geophys. Res.*, **112**(F4), F04007 (doi: 10.1029/2006JF000731)
- Hambrey MJ and Müller F (1978) Structures and ice deformation in the White Glacier, Axel Heiberg Island, Northwest Territories, Canada. *J. Glaciol.*, **20**(82), 41–66
- Hammann AC and Sandhäger H (2006) Propagation of cracks through an ice shelf as precondition for calving: numerical experiments with an idealised glacial system. *FRISP Rep.* 14, 1–6
- Holdsworth G (1969) Primary transverse crevasses. *J. Glaciol.*, **8**(52), 107–129
- Holdsworth G (1977) Tidal interaction with ice shelves. *Ann. Géophys.*, **33**(1/2), 133–146
- Holland PR, Corr HFJ, Vaughan DG, Jenkins A and Skvarca P (2009) Marine ice in Larsen Ice Shelf. *Geophys. Res. Lett.*, **36**(11), L11604 (doi: 10.1029/2009GL038162)
- Hughes T (1977) West Antarctic ice streams. *Rev. Geophys. Space Phys.*, **15**(1), 1–46
- Hughes T (1983) On the disintegration of ice shelves: the role of fracture. *J. Glaciol.*, **29**(101), 98–117
- Hughes T (1989) Calving ice walls. *Ann. Glaciol.*, **12**, 74–80
- Hulbe CL, Ledoux C and Cruikshank K (2010) Propagation of long fractures in the Ronne Ice Shelf, Antarctica, investigated using a numerical model of fracture propagation. *J. Glaciol.*, **56**(197), 459–472
- Humbert A and Steinhage D (2011) The evolution of the western rift area of the Fimbul Ice Shelf, Antarctica. *Cryosphere*, **5**(4), 931–944
- Humbert A, Kleiner T, Mohrholz C-O, Oelke C, Greve R and Lange MA (2009) A comparative modeling study of the Brunt Ice Shelf/Stancomb-Wills Ice Tongue system, East Antarctica. *J. Glaciol.*, **55**(189), 53–65
- Jansen D, Kulesa B, Sammonds PR, Luckman A, King EC and Glasser NF (2010) Present stability of the Larsen C ice shelf, Antarctic Peninsula. *J. Glaciol.*, **56**(198), 593–600
- Jenkins A and Holland D (2007) Melting of floating ice and sea level rise. *Geophys. Res. Lett.*, **34**(16), L16609 (doi: 10.1029/2007GL030784)
- Jezeq KC and Bentley CR (1983) Field studies of bottom crevasses in the Ross Ice Shelf, Antarctica. *J. Glaciol.*, **29**(101), 118–126
- Jezeq KC, Farness K, Carande R, Wu X and Labelle-Hamer N (2003) RADARSAT 1 synthetic aperture radar observations of Antarctica: Modified Antarctic Mapping Mission, 2000. *Radio Sci.*, **38**(4), 8067 (doi: 10.1029/2002RS002643)
- Joughin I (2002) Ice-sheet velocity mapping: a combined interferometric and speckle-tracking approach. *Ann. Glaciol.*, **34**, 195–201
- Joughin I and Alley RB (2011) Stability of the West Antarctic ice sheet in a warming world. *Nature Geosci.*, **4**(8), 506–513
- Joughin I and MacAyeal DR (2005) Calving of large tabular icebergs from ice shelf rift systems. *Geophys. Res. Lett.*, **32**(2), L02501 (doi: 10.1029/2004GL020978)
- Joughin I and Padman L (2003) Melting and freezing beneath Filchner–Ronne Ice Shelf, Antarctica. *Geophys. Res. Lett.*, **30**(9), 1477–1480
- Joughin I, Abdalati W and Fahnestock MA (2004) Large fluctuations in speed on Greenland's Jakobshavn Isbræ glacier. *Nature*, **432**(7017), 608–610
- Kenneally JP and Hughes TJ (2002) The calving constraints on inception of Quaternary ice sheets. *Quat. Int.*, **95–96**, 43–53
- Kenneally JP and Hughes TJ (2004) Fracture and back stress along the Byrd Glacier flowband on the Ross Ice Shelf. *Antarct. Sci.*, **16**(3), 345–354
- Kenneally JP and Hughes T (2006) Calving giant icebergs: old principles, new applications. *Antarct. Sci.*, **18**(3), 409–419
- Khazendar A, Rignot E and Larour E (2007) Larsen B Ice Shelf rheology preceding its disintegration inferred by a control method. *Geophys. Res. Lett.*, **34**(19), L19503 (doi: 10.1029/2007GL030980)
- Khazendar A, Rignot E and Larour E (2009) Roles of marine ice, rheology, and fracture in the flow and stability of the Brunt/Stancomb-Wills Ice Shelf. *J. Geophys. Res.*, **114**(F4), F04007 (doi: 10.1029/2008JF001124)
- Larour E, Rignot E and Aubry D (2004a) Modelling of rift propagation on Ronne Ice Shelf, Antarctica, and sensitivity to climate change. *Geophys. Res. Lett.*, **31**(16), L16404 (doi: 10.1029/2004GL020077)
- Larour E, Rignot E and Aubry D (2004b) Processes involved in the propagation of rifts near Hemmen Ice Rise, Ronne Ice Shelf, Antarctica. *J. Glaciol.*, **50**(170), 329–341
- Lawn BR (1993) *Fracture of brittle solids*, 2nd edn. Cambridge University Press, Cambridge
- Le Brocq AM, Payne AJ and Vieli A (2010) An improved Antarctic dataset for high resolution numerical ice sheet models (ALBMAP v1). *Earth Syst. Sci. Data*, **2**(2), 247–260
- Levermann A, Albrecht T, Winkelmann R, Martin MA, Haseloff M and Joughin I (2011) Kinematic first-order calving law implies potential for abrupt ice-shelf retreat. *Cryos. Discuss.*, **5**(5), 2699–2722
- Lingle CS, Hughes TJ and Kollmeyer RC (1981) Tidal flexure of Jakobshavn's Glacier, West Greenland. *J. Geophys. Res.*, **86**(B5), 3960–3968
- Luckman A, Jansen D, Kulesa B, King EC, Sammonds P and Benn DI (2011) Basal crevasses in Larsen C Ice Shelf and implications for their global abundance. *Cryos. Discuss.*, **5**(4), 2035–2060
- Lythe MB, Vaughan DG and BEDMAP consortium (2001) BEDMAP: a new ice thickness and subglacial topographic model of Antarctica. *J. Geophys. Res.*, **106**(B6), 11 335–11 351
- Ma Y, Gagliardini O, Ritz C, Gillet-Chaulet F, Durand G and Montagnat M (2010) Enhancement factors for grounded ice and ice shelves inferred from an anisotropic ice-flow model. *J. Glaciol.*, **56**(199), 805–812
- MacAyeal DR (1989) Large-scale ice flow over a viscous basal sediment: theory and application to Ice Stream B, Antarctica. *J. Geophys. Res.*, **94**(B4), 4071–4087
- MacAyeal DR, Scambos TA, Hulbe CL and Fahnestock MA (2003) Catastrophic ice-shelf break-up by an ice-shelf-fragment-capsize mechanism. *J. Glaciol.*, **49**(164), 22–36
- Martin MA and 6 others (2011) The Potsdam Parallel Ice Sheet Model (PISM-PIK) – Part 2: dynamic equilibrium simulation of the Antarctic ice sheet. *Cryosphere*, **5**(3), 727–740

- Morland LW (1987) Unconfined ice-shelf flow. In Van der Veen CJ and Oerlemans J eds. *Dynamics of the West Antarctic ice sheet*. D. Reidel, Dordrecht, 99–116
- Morton KW and Mayers DF (2005) *Numerical solution of partial differential equations: an introduction*, 2nd edn. Cambridge University Press, Cambridge
- Nath PC and Vaughan DG (2003) Subsurface crevasse formation in glaciers and ice sheets. *J. Geophys. Res.*, **108**(B1), 2020 (doi: 10.1029/2001JB000453)
- Nye JF (1952) The mechanics of glacier flow. *J. Glaciol.*, **2**(12), 82–93
- Paterson MS and Wong T-F (2005) *Experimental rock deformation – the brittle field*, 2nd edn. Springer-Verlag, Berlin
- Payne AJ, Vieli A, Shepherd A, Wingham DJ and Rignot E (2004) Recent dramatic thinning of largest West Antarctic ice stream triggered by oceans. *Geophys. Res. Lett.*, **31**(23), L23401 (doi: 10.1029/2004GL021284)
- PISM group (2011) *PISM, a parallel ice sheet model: user's manual*. <http://www.pism-docs.org>
- Pralong A and Funk M (2005) Dynamic damage model of crevasse opening and application to glacier calving. *J. Geophys. Res.*, **110**(B1), B01309 (doi: 10.1029/2004JB003104)
- Pralong A, Hutter K and Funk M (2006) Anisotropic damage mechanics for viscoelastic ice. *Contin. Mech. Thermodyn.*, **17**(5), 387–408
- Rack W and Rott H (2004) Pattern of retreat and disintegration of the Larsen B ice shelf, Antarctic Peninsula. *Ann. Glaciol.*, **39**, 505–510
- Reeh N (1968) On the calving of ice from floating glaciers and ice shelves. *J. Glaciol.*, **7**(50), 215–232
- Rignot E (2006) Changes in ice dynamics and mass balance of the Antarctic ice sheet. *Philos. Trans. R. Soc. London, Ser. A*, **364**(1844), 1637–1655
- Rignot E, Casassa G, Gogineni P, Krabill W, Rivera A and Thomas R (2004) Accelerated ice discharge from the Antarctic Peninsula following the collapse of Larsen B ice shelf. *Geophys. Res. Lett.*, **31**(18), L18401 (doi: 10.1029/2004GL020697)
- Rignot E and 6 others (2008) Recent Antarctic ice mass loss from radar interferometry and regional climate modelling. *Nature Geosci.*, **1**(2), 106–110
- Rist MA, Sammonds PR, Murrell SAF, Meredith PG, Oerter H and Doake CSM (1996) Experimental fracture and mechanical properties of Antarctic ice: preliminary results. *Ann. Glaciol.*, **23**, 284–292
- Rist MA and 6 others (1999) Experimental and theoretical fracture mechanics applied to Antarctic ice fracture and surface crevassing. *J. Geophys. Res.*, **104**(B2), 2973–2987
- Rist MA, Sammonds PR, Oerter H and Doake CSM (2002) Fracture of Antarctic shelf ice. *J. Geophys. Res.*, **107**(B1) (doi: 10.1029/2000JB000058)
- Rott H, Skvarca P and Nagler T (1996) Rapid collapse of northern Larsen Ice Shelf, Antarctica. *Science*, **271**(5250), 788–792
- Rott H, Rack W, Skvarca P and De Angelis H (2002) Northern Larsen Ice Shelf, Antarctica: further retreat after collapse. *Ann. Glaciol.*, **34**, 277–282
- Rott H, Rack W and Nagler T (2007) Increased export of grounded ice after the collapse of Northern Larsen Ice Shelf, Antarctic Peninsula, observed by Envisat ASAR. In Lacoste H and Ouwehand L eds. *IGARSS '07, International Geoscience and Remote Sensing Symposium, 23–27 July 2007, Barcelona, Spain, Vol. 3*. Institute of Electrical and Electronics Engineers, Piscataway, NJ, 1174–1176
- Rott H, Müller F, Nagler T and Floricioiu D (2011) The imbalance of glaciers after disintegration of Larsen-B ice shelf, Antarctic Peninsula. *Cryosphere*, **5**(1), 125–134
- Saheicha K, Sandhäger H and Lange MA (2006) Modelling the flow regime of Filchner-Schelfeis. *FRISP Rep.* 14, 58–62,
- Sandhäger H, Rack W and Jansen D (2005) Model investigations of Larsen B Ice Shelf dynamics prior to the breakup. *FRISP Rep.* 16, 5–12
- Sassolas C, Pfeffer T and Amadei B (1996) Stress interaction between multiple crevasses in glacier ice. *Cold Reg. Sci. Technol.*, **24**(2), 107–116
- Scambos TA, Hulbe C, Fahnestock M and Bohlander J (2000) The link between climate warming and break-up of ice shelves in the Antarctic Peninsula. *J. Glaciol.*, **46**(154), 516–530
- Scambos TA, Bohlander JA, Shuman CA and Skvarca P (2004) Glacier acceleration and thinning after ice shelf collapse in the Larsen B embayment, Antarctica. *Geophys. Res. Lett.*, **31**(18), L18402 (doi: 10.1029/2004GL020670)
- Scambos T and 7 others (2009) Ice shelf disintegration by plate bending and hydro-fracture: satellite observations and model results of the 2008 Wilkins ice shelf break-ups. *Earth Planet. Sci. Lett.*, **280**(1–4), 51–60
- Schmeltz M, Rignot E, Dupont TK and MacAyeal DR (2002) Sensitivity of Pine Island Glacier, West Antarctica, to changes in ice-shelf and basal conditions: a model study. *J. Glaciol.*, **48**(163), 552–558
- Shepherd A and Wingham D (2007) Recent sea-level contributions of the Antarctic and Greenland ice sheets. *Science*, **315**(5818), 1529–1532
- Shepherd A, Wingham D, Wallis D, Giles K, Laxon S and Sundal AV (2010) Recent loss of floating ice and the consequent sea level contribution. *Geophys. Res. Lett.*, **37**(13), L13503 (doi: 10.1029/2010GL042496)
- Skrzypczek JJ and Ganczarski A (1999) *Modeling of material damage and failure of structures: theory and applications*. Springer-Verlag, Berlin
- Smith RA (1976) The application of fracture mechanics to the problem of crevasse penetration. *J. Glaciol.*, **17**(76), 223–228
- Thomas RH, Rignot E, Kanagaratnam K, Krabill WB and Casassa G (2004) Force-perturbation analysis of Pine Island Glacier, Antarctica, suggests cause for recent acceleration. *Ann. Glaciol.*, **39**, 133–138
- Van der Veen CJ (1998a) Fracture mechanics approach to penetration of bottom crevasses on glaciers. *Cold Reg. Sci. Technol.*, **27**(3), 213–223
- Van der Veen CJ (1998b) Fracture mechanics approach to penetration of surface crevasses on glaciers. *Cold Reg. Sci. Technol.*, **27**(1), 31–47
- Van der Veen CJ (1999) *Fundamentals of glacier dynamics*. A.A. Balkema, Rotterdam
- Van der Veen CJ (2007) Fracture propagation as means of rapidly transferring surface meltwater to the base of glaciers. *Geophys. Res. Lett.*, **34**(1), L01501 (doi: 10.1029/2006GL028385)
- Vaughan DG (1993) Relating the occurrence of crevasses to surface strain rates. *J. Glaciol.*, **39**(132), 255–266
- Vieli A, Payne AJ, Du Z and Shepherd A (2006) Numerical modelling and data assimilation of the Larsen B ice shelf, Antarctic Peninsula. *Philos. Trans. R. Soc. London, Ser. A*, **364**(1844), 1815–1839
- Vieli A, Payne AJ, Shepherd A and Du Z (2007) Causes of pre-collapse changes of the Larsen B ice shelf: numerical modelling and assimilation of satellite observations. *Earth Planet. Sci. Lett.*, **259**(3–4), 297–306
- Weertman J (1973) Can a water-filled crevasse reach the bottom surface of a glacier? *IASH Publ.* 95 (Symposium at Cambridge 1969 – *Hydrology of Glaciers*), 139–145
- Weertman J (1977) Penetration depth of closely spaced water-free crevasses. *J. Glaciol.*, **18**(78), 37–46
- Weertman J (1980) Bottom crevasses. *J. Glaciol.*, **25**(91), 185–188
- Weertman J (1996) *Dislocation based fracture mechanics*. World Scientific, Singapore
- Weiss J (2004) Subcritical crack propagation as a mechanism of crevasse formation and iceberg calving. *J. Glaciol.*, **50**(168), 109–115
- Winkelmann R and 6 others (2011) The Potsdam Parallel Ice Sheet Model (PISM-PIK) – Part 1: model description. *Cryosphere*, **5**(3), 715–726

APPENDIX

PISM-PIK

The fracture-density parameterization was implemented in the Potsdam Parallel Ice Sheet Model, PISM-PIK, which is based on the thermomechanically coupled open-source Parallel Ice Sheet Model stable 0.2 (Bueler and Brown, 2009; PISM group, 2011). Most modifications of PISM, as described by Winkelmann and others (2011), concern the ice-shelf dynamics and have been tested in simulations of the Antarctic ice sheet forced with present-day boundary conditions (Martin and others, 2011). Most modifications are now merged into PISM stable 0.4. Solving the discretized stress balance in the SSA (Morland, 1987; MacAyeal, 1989) with appropriate boundary conditions, especially at the calving front, yields vertically integrated velocities. Calculations run in parallel using the Portable, Extensible Toolkit for Scientific computation (PETSc; Balay and others, 2008). Transport of fracture density on the fixed rectangular grid is approximated with a first-order upwind scheme based on a finite-volume method (Morton and Mayers, 2005). Time-stepping is explicit and adaptive. The code applies a subgrid representation of the calving front, as introduced by Albrecht and others (2011).

Computational set-up

In our experiments we used four different computational set-ups. For parameter studies, simple geometries, such as an ice shelf confined in a rectangular bay with unidirectional inflow, are used. For (1) a narrow embayment of 150 km width and 250 km length and (2) a wide bay of 300 km width and 150 km length (Fig. 2) we define Dirichlet boundary conditions for the vertically averaged velocity in SSA as a distribution $u(x_0)$ with $u_{\max}(x_0) = 10^{-5} \text{ m s}^{-1}$ in the center, decaying to zero at the sides with the fourth power (for flow law exponent $n = 3$, as in Dupont and Alley, 2006, eqn (6)), shown as a gray curve in the upper right panels of Figure 3a and b. The ice thickness at this boundary position is constant, $H(x_0) = 600 \text{ m}$, and for fracture density we assume $\phi(x_0) = \phi_0 = 0.1$. Mean annual surface temperature is $T = 247 \text{ K}$ and the base is at pressure-melting temperature. Melting and accumulation are not considered here. Along the bedrock-side friction is prescribed by a viscosity of $\eta_B = 5 \times 10^{13} \text{ Pa s}$, which is more realistic than forcing boundary velocities to zero. At the ice-shelf front, ice calves off at ice thickness 175 m. The quadratic set-up measures 201×201 gridcells of 2500 m length each. Vertical levels are unequally spaced, on average 6 m thick.

Simulation set-ups with realistic topography are used for comparison with observational data. For (3) the FRIS, data

from the SeaRISE dataset defined on a 5 km grid (Le Brocq and others, 2010) were applied on a 201×201 mesh. The lateral boundaries of the ice shelf are inferred according to bed topography and flotation criterion applied to the ice thickness. Only floating ice was modeled.

At the inlets, Dirichlet boundary conditions for the SSA-velocity calculation were defined on the basis of observed velocities, determined using interferometric synthetic aperture radar (InSAR) and speckle tracking (Joughin, 2002; Joughin and Padman, 2003). Boundary positions at the inlets have been adjusted to locations where velocity data were available. Hence their position varies partly compared with the grounding line in the overlaid data of Hulbe and others (2010). Vertical levels are equally spaced with $\Delta z = 35 \text{ m}$. Mean annual surface temperature was adopted accordingly (Comiso, 2000) and ranges from -24°C to -19°C ; basal temperature is at pressure-melting point. Neither basal melting nor accumulation is applied in these experiments; the ice thickness is prescribed.

As a second example (4) we model the significantly smaller northern Larsen Ice Shelf fringing the Antarctic Peninsula between 64.5°S and 66°S . The small ice shelves fringing the large ice sheets are of essential concern, since they reveal a strong buttressing effect on the tributaries and seem to be much more sensitive to changing climatic boundary conditions. We prepared a computational set-up of Larsen A+B on a regular 201×201 mesh with all data regridded to 1 km resolution. Surface elevation and velocity data have been raised in the Modified Antarctic Mapping Mission (MAMM) by the Byrd Center group (Jezek and others, 2003), based on observations of the years 1997–2000 (before the catastrophic disintegration event in Larsen B), provided on a 2 km grid in polar stereographic projection grid by Dave Covey of the University of Alaska Fairbanks. Gaps in the data were filled by averaging over neighboring gridcells. Ice-shelf thickness is calculated from surface elevation, assuming a firn-corrected hydrostatic relation (Lythe and others, 2001, eqn (2)).

Grounding line position is assumed to be located where the surface gradient exceeds a critical value (also for ice rises). Reconstructed velocities and ice thicknesses were set as a Dirichlet boundary condition at the grounding line in inlet regions, simulating the ice-stream inflow through the mountains. The annual mean surface temperature data were taken from the present-day Antarctica SeaRISE dataset, available on a 5 km grid (Comiso, 2000; Le Brocq and others, 2010), regridded to 1 km resolution, ranging from -13°C to -11°C . Accumulation and basal melting are neglected, since ice thickness is prescribed in our experiments to reduce tuning parameters.

MS received 11 September 2011 and accepted in revised form 3 November 2011